Geophysical Journal International

Geophys. J. Int. (2013) **192,** 441–455 doi: 10.1093/gji/ggs032

Present kinematics of the Tjörnes Fracture Zone, North Iceland, from campaign and continuous GPS measurements

Sabrina Metzger,[1] Sigurjón Jónsson,[2] Gillis Danielsen,[2] Sigrún Hreinsdóttir,[3] François Jouanne,[4] Domenico Giardini[1] and Thierry Villemin[4]

[1]*Institute of Geophysics, ETH Zürich, Sonneggstrasse* 5, 8092 *Zürich, Switzerland. E-mail: smetzger@erdw.ethz.ch*
[2]*King Abdullah University of Science and Technology (KAUST), Thuwal, Saudi Arabia*
[3]*Nordic Volcanological Center, Institute of Earth Sciences, University of Iceland, Iceland*
[4]*Université de Savoie, Bourget-du-Lac, France*

Accepted 2012 October 17. Received 2012 October 8; in original form 2012 March 29

SUMMARY

The Tjörnes Fracture Zone (TFZ), North Iceland, is a 120 km transform offset of the Mid-Atlantic-Ridge that accommodates 18 mm yr^{-1} plate motion on two parallel transform structures and connects the offshore Kolbeinsey Ridge in the north to the on-shore Northern Volcanic Zone (NVZ) in the south. This transform zone is offshore except for a part of the right-lateral strike-slip Húsavík-Flatey fault (HFF) system that lies close to the coastal town of Húsavík, inducing a significant seismic risk to its inhabitants. In our previous work we constrained the locking depth and slip-rate of the HFF using 4 yr of continuous GPS measurements and found that the accumulated slip-deficit on the fault is equivalent to a M_w6.8 ± 0.1 earthquake, assuming a complete stress release in the last major earthquakes in 1872 and a steady accumulation since then.

In this paper we improve our previous analysis by adding 44 campaign GPS (EGPS) data points, which have been regularly observed since 1997. We extract the steady-state interseismic velocities within the TFZ by correcting the GPS data for volcanic inflation of Theistareykir—the westernmost volcano of the NVZ—using a model with a magma volume increase of 25 × 10^6 m^3, constrained by InSAR time-series analysis results.

The improved velocity field based on 58 GPS stations confirms the robustness of our previous model and allows to better constrain the free model parameters. For the HFF we find a slightly shallower locking depth of ∼6.2 km and a slightly higher slip-rate of ∼6.8 mm yr^{-1} that again result in the same seismic potential equivalent to a M_w6.8 earthquake. The much larger number of GPS velocities improves the statistically estimated model parameter uncertainties by a factor of two, when compared to our previous study, a result that we validate using Bayesian estimation.

Key words: Time series analysis; Numerical approximations and analysis; Satellite geodesy, Radar interferometry; Oceanic transform and fracture zone processes; Kinematics of crustal and mantle deformation.

1 INTRODUCTION

The Tjörnes Fracture Zone (TFZ) in North Iceland, is one of two transform zones in Iceland that can produce magnitude ∼7 strike-slip earthquakes with a recurrence interval of decades to centuries (Einarsson 1991). Due to its mostly offshore location and its complex geometry, consisting of at least two parallel transform structures, the detailed tectonics and kinematics of this plate boundary zone are still not well understood. One of the main lineaments in the fracture zone, the Húsavík-Flatey fault (HFF), has ruptured in major earthquakes in 1755 and 1872, which indicates that the interseismic period of the earthquake cycle might end soon. It is therefore important to estimate the seismic potential of this strike-slip fault and its implications for the inhabitants of Húsavík, a town located right on top of the fault. One way to assess the seismic potential of a locked fault is to estimate the dimensions of the locked fault plane (length and locking depth) and the accumulated slip deficit since the last major earthquake, derived from interseismic deformation rates (Wesnousky 1986).

Several studies have provided information about the slip rate and the locking depth of the HFF. An estimation of max. 60 km accumulated slip during the last 7–9 Myr from Sæmundsson (1974) and Gudmundsson *et al.* (1993) results in an average slip rate of a max. 7–8 mm yr^{-1}. Rögnvaldsson *et al.* (1998) analysed relative locations of 1400 earthquakes in 60 swarms within the TFZ 1994–1997 with a vertical uncertainty <2 km and found that less than 10 per cent of all

events occur deeper than 10 km, deducing a base of the brittle crust at 10 km. Velocities from the first three continuous GPS stations in North Iceland that were installed in 2001–2002 suggest that the HFF accommodates 40 per cent of the total plate motion (Geirsson *et al.* 2006). Using a plate spreading velocity of 18 mm yr^{-1} (MORVEL, DeMets *et al.* 2010) this corresponds to a slip rate of 7 mm yr^{-1}. Other slip rates derived from campaign GPS data are in the range of ∼5 mm yr^{-1} (Árnadóttir *et al.* 2009) to 8 mm yr^{-1} (Jouanne *et al.* 2006). In addition, Árnadóttir *et al.* (2009) used modelling to constrain the locking depth of the HFF at shallow 5 km, but the data used were sparse near the HFF and thus the locking depth was poorly constrained.

In our previous study, we presented data from 14 continuous GPS (CGPS) stations in North Iceland, most of which we installed in 2006 to monitor the surface deformation within the TFZ (Metzger *et al.* 2011). We modelled the kinematics of the plate boundary in North Iceland with an interseismic back-slip model based on nine dislocations in an elastic half-space plus a Mogi source representing inflation of the Theistareykir volcano (Fig. 1). Our aim was to estimate both the locking depth and the slip rate of the HFF. We found a slip rate of 6.6 ± 0.6 mm yr^{-1} and a surprisingly shallow locking depth of $6.3^{+1.7}_{-1.2}$ km. Furthermore, the modelling revealed that the HFF accommodates only 34 ± 3 per cent of the total plate motion, while the majority of the transform motion must be taken up by the offshore Grímsey Oblique Rift (GOR), the other main lineament of the TFZ. Assuming complete stress unloading in the last major earthquakes in 1872 and steady stress accumulation since then, the seismic potential of a complete rupture of the HFF corresponds to a M_w6.8 ± 0.1 event (Metzger *et al.* 2011).

In this paper, we improve the kinematic model of the Tjörnes Fracture Zone by adding 44 campaign GPS (EGPS) observations to the 14 CGPS data to further constrain the model parameters of the TFZ. In addition, we analyse the time evolution of the transient volcanic uplift at Theistareykir using InSAR time-series analysis and remove this signal from the GPS data to obtain corrected interseismic deformation rates. Due to the enhanced network density near the onshore part of HFF and across the rift zone along the Krafla system we are able to better constrain all model parameters. After an overview section of the tectonic setting in North Iceland we present a review of historical earthquakes in the region. We

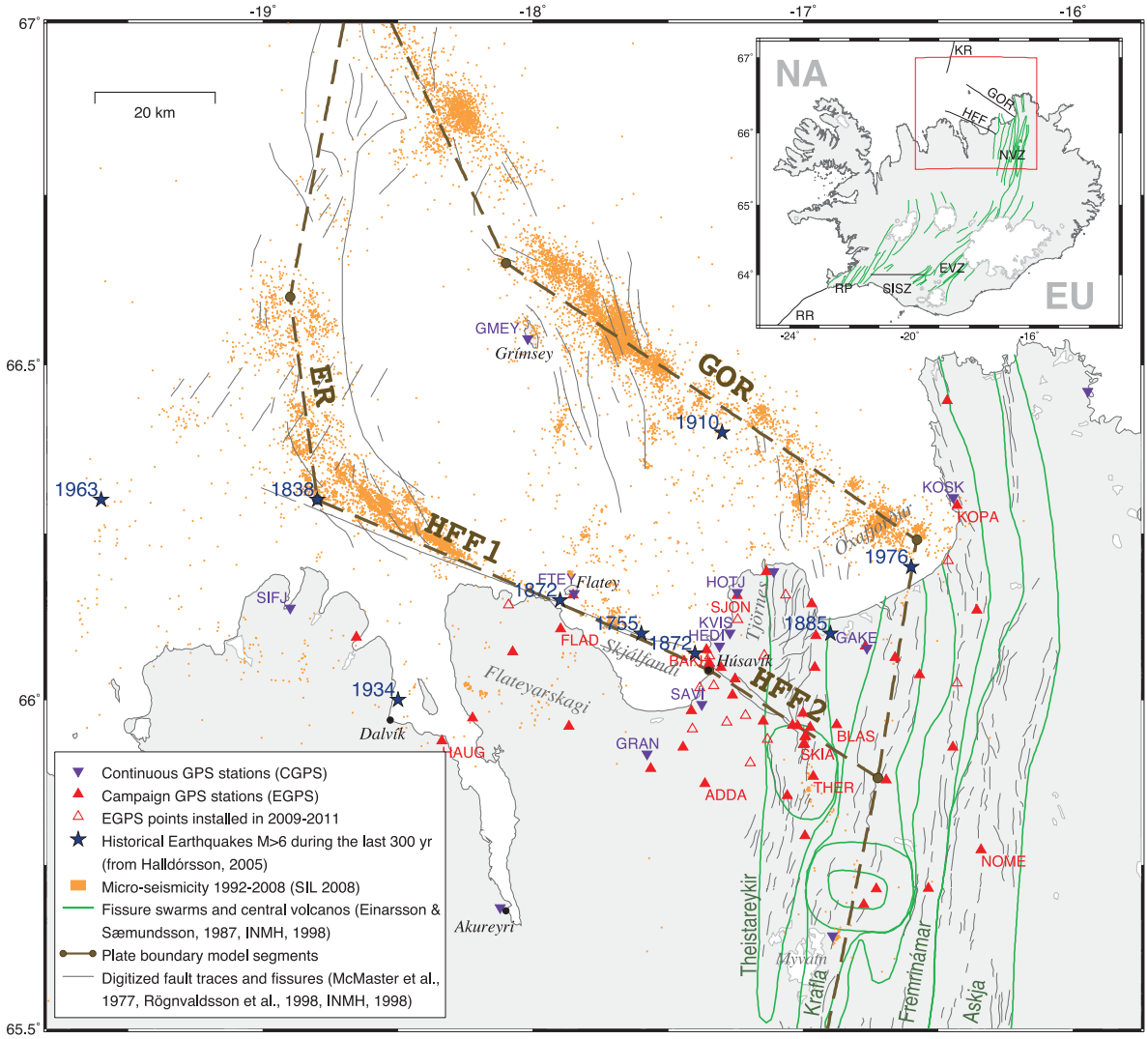

Figure 1. Tectonic setting, seismicity and GPS markers in North Iceland. The mid-Atlantic Ridge separates the North American (NA) and the Eurasian plate (EU) and is offset by the South Icelandic Seismic Zone in the South (SISZ) and by the Húsavík-Flatey Fault (HFF) and the Grímsey Oblique Rift (GOR) in the North (inset). Other plate boundary segments: ER, Eyjafjarðaráll Rift; EVZ, Eastern Volcanic Zone; KR, Kolbeinsey Ridge; NVZ, Northern Volcanic Zone; RP, Reykjanes Peninsula; RR, Reykjanes Ridge. The station labels refer to Fig. 5.

then document the acquisition and processing of the campaign GPS data, explain how we resolve the transient deformation signal using InSAR time-series analysis, and how we estimate the steady interseismic velocities from both the EGPS and CGPS time-series. The last part of this paper explains how we model the kinematics of the TFZ and derive best-fitting model parameters and their uncertainties using two different approaches of uncertainty estimation. Finally, the obtained results are discussed and compared with earlier published kinematic parameters.

2 TECTONIC SETTING OF NORTH ICELAND

Iceland is located on the mid-Atlantic Ridge where the Eurasian and North American Plate are separating at a rate of 18 mm yr^{-1} in a N104.5°E direction, according to the MORVEL plate-motion model (DeMets *et al.* 2010). The plate boundary zone in Iceland is a few tens of kilometre wide, crossing the island from the southwest to the northeast, and is mostly defined by volcanic zones [i.e. the western, eastern and Northern Volcanic Zones (NVZ)] that accommodate the spreading motion within several parallel and overlapping volcanic systems (Fig. 1). However the onshore part of the plate boundary is offset ∼100 km towards east, resulting in two transform zones at the southern and the northern shore of the island. The southern transform zone is called the South Iceland Seismic Zone and connects Reykjanes peninsula, a continuation of the Reykjanes Ridge, to the Eastern Volcanic Zone. It is completely onshore and consists of a series of parallel N–S trending strike-slip faults, sometimes referred to as *bookshelf faulting* (Einarsson 1991). The Northern transform zone is usually called the Tjörnes Fracture Zone (TFZ) and is of a completely different geometry. It consists of the 100-km-long HFF and a second lineament located northeast of the HFF, the Grímsey Oblique Rift (GOR), that both connect the NVZ to the Kolbeinsey Ridge (KR).

The plate boundary structures in the TFZ are primarily marked by fault surface traces and microseismicity. The HFF is a mostly off-shore strike-slip fault with a minor opening component. The WNW-oriented 90-km-long main fault strand extends from the Theistareykir fissure swarm to the Eyjafjarðaráll Rift. This rift links the HFF and the Kolbeinsey Ridge, which is the northward continuation of the mid-Atlantic Ridge (Fig. 1). The HFF has been active for as long as 7–9 Myr with an estimated cumulative displacement of max. 60 km and is older than the GOR (Sæmundsson 1974; Gudmundsson *et al.* 1993; Homberg *et al.* 2010). Fault surface traces between the coastal town Húsavík and the Theistareykir fissure swarm show several parallel branches and a slight bend at Húsavík leading to a NW-strike of the onshore part of the fault system. This change in strike results in an increasing opening component of the fault system, which is expressed in pull-apart structures (*sag ponds*) southeast of Húsavík. The southeastern part of the fault lacks microseismicity, particularly since the Krafla rifting-episode 1975–1984 (Tryggvason 1980, 1984; Björnsson 1985). One possible explanation for the low microseismicity is that the rifting episode released accumulated stress on the southeastern part of the HFF (Maccaferri *et al.* 2012).

The second main lineament in the TFZ is the Grímsey Oblique Rift. It is similar to the Reykjanes Peninsula in southwest Iceland, consisting of a set of parallel, N–S oriented faults exhibiting both normal and strike-slip faulting and it is volcanically active (Rögnvaldsson *et al.* 1998). In our previous work we estimated that 66 ± 3 per cent of the total TFZ transform motion is accommodated by the GOR (Metzger *et al.* 2011) where as the rest is taken up by the HFF.

The NVZ is a 40 km wide rift zone that extends from Vatnajökull glacier in Southeast Iceland to the north coast and the TFZ, consisting of five volcanic systems (from NNW to SSE): Theistareykir, Krafla, Fremrinámar, Askja and Kverkfjöll (Fig. 1). It became active 7–9 Myr after an eastward jump of the plate boundary (Sæmundsson 1974). The most recent rifting episode within the NVZ took place in the Krafla volcanic system in 1975–1984 (Tryggvason 1980, 1984; Björnsson 1985) with over 20 intrusive events and crustal widening amounting to an average of 5 m across the Krafla fissure swarm, corresponding to 275 yr of plate spreading (Tryggvason 1994). After 9 yr the rifting episode stopped, but the extensional pulse continued to propagate away from the rift axis and over time slowly decayed in amplitude (Foulger *et al.* 1992; Heki *et al.* 1993; Hofton & Foulger 1996). Fifteen years later the influence of the rifting episode had diminished (Völksen 2000). Other recent rifting episodes in the NVZ occurred in the Krafla volcanic system 1724–1729 and Askja volcanic system 1874–1875 (Sigurdsson & Sparks 1978). Two minor rifting events took place in 1618 and 1885 in Theistareykir, the westernmost volcanic system in the NVZ (Magnúsdóttir & Brandsdóttir 2011). Theistareykir has not erupted since 2500 BP (Karl Grönvold 2011, personal communication) but between 2007 and 2009 it had a period of inflation with a maximum uplift rate of ∼3 cm yr^{-1} in late 2008 (see Section 5.1).

3 HISTORICAL EARTHQUAKES IN THE TJÖRNES FRACTURE ZONE

Knowledge of large historical earthquakes provides vital information on the average length of the earthquake cycle. The first instrumentally derived magnitude and location estimations of Icelandic earthquakes were available in the beginning of the last century. For older events we have to rely on historical accounts, which are far from being complete, and treat the available information with caution. Information on historical earthquakes in North Iceland dates back to 1260, when a large earthquake took place close to Flatey island (Fig. 1, Thoroddsen 1880, 1925), but accounts from the following 3–4 centuries are limited (Thorgeirsson 2012). Below we list the largest known earthquakes in the TFZ during the past 300 yr with magnitude estimates as given in (Stefánsson *et al.* 2008).

In 1755 a *M*7 earthquake took place in Skjálfandi Bay, which was felt widely on Tjörnes Peninsula as well as on the two peninsulas west of Skjálfandi Bay and caused damage to many buildings, open cracks and rock fall along the fjords (Thoroddsen 1925). Another earthquake happened near the northwestern end of the HFF in 1838 (*M*6.5). The next two large earthquakes on the HFF occurred 6 hr apart in 1872 and the size of each has been estimated *M*6.5. The former event took place near Húsavík, causing fissures with up to 1 m of opening (Thoroddsen 1925, p. 400), but the latter occurred close to Flatey island. Other major events were the *M*6.2 earthquake close to the town of Dalvík in 1934 and a *M*7 earthquake in 1963 that was located ∼60 km northwest of Dalvík. Due to these two large events and some microseismicity Einarsson (1976) have suggested a third 'weak' Dalvík zone southwest of the HFF with several N–S trending faults, similar to the Grímsey Oblique Rift.

Known large earthquakes along the Grímsey Oblique Rift are a M6.3 earthquake in 1885 induced by the Theistareykir rifting event at that time, a M7 earthquake in 1910 midway between the island Grímsey and Öxarfjördur and a M6.2 earthquake in 1976 at the northern end of the Krafla fissure swarm. The last one mentioned

was part of the initial phase of the Krafla rifting episode 1975–1984 (Tryggvason 1980; Björnsson 1985; Tryggvason 1984; Passarelli *et al.* 2012).

In order to estimate the seismic potential of the HFF we assume that during the last 250 years only three major earthquakes in 1755 and 1872 ruptured substantial parts of HFF. This indicates that the next big event might be due soon. We furthermore assume that the stress regime on the HFF was completely relaxed in the last two earthquakes of 1872 and that the slip deficit of the fault has steadily increased since then.

4 GPS DATA

The first GPS reference markers were installed in North Iceland in 1987 to study the post-rifting relaxation after the Krafla rifting episode 1975–1984 (Foulger *et al.* 1992; Heki *et al.* 1993). This network was remeasured several times in the following years (1990, 1992, 1995) to analyse the influence of the rifting episode and the return to steady-state deformation (Hofton & Foulger 1996; Völksen 2000. Another, partially overlapping network was installed in 1995 to study the TFZ and it has been remeasured completely five times (1997/1999/2002/2007/2010) and partially on several occasions (2000/2001/2005/2009/2011), that is, mostly the GPS markers close to Húsavík (Jouanne *et al.* 1999, 2006). 15 new campaign GPS points were added in 2009–2011 to improve the GPS station density near the HFF. Today the TFZ GPS network consists of 14 continuous and 61 campaign GPS stations (Fig. 1, Table 3).

4.1 GPS campaigns 1997–2011

During GPS campaigns, each point was typically measured for two consecutive nights, except in 1997, when the observation time was somewhat shorter (∼24 hr). The GPS antennas were aligned to magnetic north in the earlier campaigns, whereas in the 2009 campaign and after the antennas were aligned with true north using a magnetic declination of −14 degrees. The instrument types and the number of points measured differed between campaigns, see summary information in Table 1. The publication by Jouanne *et al.* (2006) provides more information about the acquisition strategy of the 1997–2007 GPS data. In 2009 we installed four new markers on the profile across the HFF and in 2010–2011 we added 11 more data points that enhance the network density north and south of the on-land part of the HFF (Fig. 1). The short time-series of these 15 points are not included in the work we present here.

Table 1. Information about the GPS campaigns 1997-2011, including the number of instruments (sets) and the number of measured points (pts). All campaigns were carried out between July and September of the given year.

Year	Receiver type	Antenna type	Sets	pts
1997	ASHTECH Z-XII3	ASH700718B/D	7	45
1999	ASHTECH Z-XII3	ASH700936B_M	4	45
	ASHTECH UZ-12		4	
2002	ASHTECH Z-XII3	ASH700936A_M	5	46
	ASHTECH UZ-12		5	
2005	ASHTECH UZ-12	ASH700936A_M		16
2007	ASHTECH UZ-12	TRM41249.00	13	40
2009	TRIMBLE NETRS	TRM41249.00	2	8
	LEICA SR530	LEIAT502	2	8
2010	ASHTECH UZ-12	TRM41249.00	10	51
2011	TRIMBLE NETR9	TRM57971.00	6	23

Table 2. Details of the GPS processing with the GAMIT-GLOBK v10.4 (Herring *et al.* 2010a,b,c) and Bernese V5.0 (Dach *et al.* 2007) software.

	GAMIT-GLOBK	BERNESE
Reference stations (IGS)	max. 19	max. 10
Reference frame	ITRF 2005	ITRF 2005
Orbits/clock files	IGS	IGS
Antenna model	Abs. phase centre	Abs. phase centre
Tropospheric corr.	Saastamoinen	Saastamoinen
Dry/wet delay mapping	GMF	NIELL
Ocean loading model	FES2004	FES2004
Cut-off-angle	10°	5°
Offset correction	Yes	Yes
Magnetic North	Yes	No (until 2007)

4.2 Data processing with GAMIT-GLOBK and BERNESE

The entire campaign GPS data set 1997–2010 was processed independently with GAMIT-GLOBK V10.4 (Herring *et al.* 2010a,b,c) and Bernese V5.0 (Dach *et al.* 2007) in order to the test robustness of the resulting GPS velocities. The details of the processing methods are given in Table 2. Both software packages constrain daily network solutions using a well-chosen set of reference (IGS) stations. In both cases we included IGS stations as well as CGPS stations in North Iceland (when available) in the data analysis and we corrected for offsets in the time-series of the continuous GPS stations due to earthquakes or antenna changes. We used the same ocean-loading model (FES2004), absolute antenna phase centre models, and the Saastamoinen model to correct for the atmospheric delay. The dry/wet delay was corrected with the GMF (in GAMIT-GLOBK) and NIELL (in BERNESE) mapping function. In the GAMIT processing we used a slightly higher cut-off-angle (10°) than in the BERNESE processing (5°).

In GPS campaigns before 2009 the antennas were aligned with magnetic north instead of true north. Since the antenna phase centre usually does not coincide with the geometrical antenna centre and can deviate quite substantially, a correction to that shift should improve the results. We corrected for this shift in the GAMIT processing but not in the BERNESE processing. In addition, during GAMIT processing we already removed data outliers in the EGPS data, whereas with BERNESE we processed all the EGPS data without restrictions. Therefore, the BERNESE results needed some post-processing visual quality control and filtering (see last part of Section 5.3).

4.3 Continuous GPS data 2006–2011

In addition to the episodic GPS (EGPS) data 1997–2010 we use velocities of 14 continuous GPS (CGPS) stations in North Iceland plus one additional station in east Iceland (HEID). The CGPS network was densified significantly from 4 to 14 stations in 2006 as we described in our previous study (Metzger *et al.* 2011). In that study we estimated the velocities with a superposition of a linear trend and a sinusoidal oscillation term. Here we have a better constrained estimation of the interseismic deformation rates due to an additional year of data and an improved correction of the transient volcanic signal of Theistareykir volcano. We explain in the following section

how we derive the interseismic deformation rates for all the GPS sites.

5 ESTIMATION OF INTERSEISMIC GPS VELOCITIES

Tectonic plates move steadily over millions of years but at plate boundaries the deformation is highly episodic. Most plate boundaries are locked for long periods of time and then suddenly become active in discrete events such as earthquakes or rifting episodes. The earthquake deformation cycle consists of slow but steady interseismic, sudden co-seismic, and transient post-seismic deformation. In rift zones as the NVZ, rifting episodes cover the average spreading of hundreds of years within relatively short rifting episodes that typically last a few years, followed by decaying post-rifting-relaxation. In addition, volcanic centres within rift zones can go through periods of inflation or deflation, which may cause transient signals in GPS time-series. In this paper, we want to extract the steady-state deformation rates within and around the TFZ, in particular the interseismic deformation rates near the HFF to constrain model parameters for the fault, so we can estimate the slip deficit of the locked HFF accumulated since the last major earthquake. This means that we have to identify and eliminate possible transient signals within the GPS time-series to isolate the linear interseismic deformation rates of the TFZ.

The Krafla rifting episode ended 25 yr ago and its effect on GPS velocities appears to have diminished before 1997 (Völksen 2000). We therefore assume that the plate-boundary deformation rates during the observation time can be approximated as linear. On the other hand, inflation at Theistareykir central volcano 2007–2009 caused a transient deformation signal at neighbouring GPS sites that we have to take into account (Metzger *et al.* 2011). In addition to tectonic signals, annual oscillation signals are visible within the continuous GPS time-series. Fig. 2 schematically shows the different components apparent in the acquired GPS time-series of the TFZ. We model the CGPS time-series using the following function:

$$f(t) = A + Bt + C\cos(2\pi t + \phi) + D\tan^{-1}\left(\frac{t - t_c}{t_d}\right), \qquad (1)$$

where $A + Bt$ represents the linear displacement rate, C the amplitude and ϕ the phase shift of annual oscillations and D the amplitude, t_c the central time and t_d the curvature factor of the transient volcanic inflation at Theistareykir central volcano. To extract the steady interseismic velocities, we have to first correct all the GPS data for the volcanic transient signal (Section 5.1) and—in case of CGPS data—annual oscillations (Section 5.2).

5.1 Uplift at Theistareykir volcano

In our previous work we detected uplift in ENVISAT interferograms at Theistareykir central volcano with a maximum uplift rate of 3 cm yr^{-1} between 2007 and 2008 (Metzger *et al.* 2011). Using both an ascending and a descending interferogram we were able to fit the spatial pattern of the inflation well with a Mogi source (Mogi 1958) and thus constrain the source location. However, the limited ENVISAT catalogue does not contain enough data to analyse well the temporal evolution of the volcanic inflation. The CGPS time-series do not provide useful information about the transient either, because they started in the midst of the inflation period and the CGPS stations are located too far away from the inflation centre. We

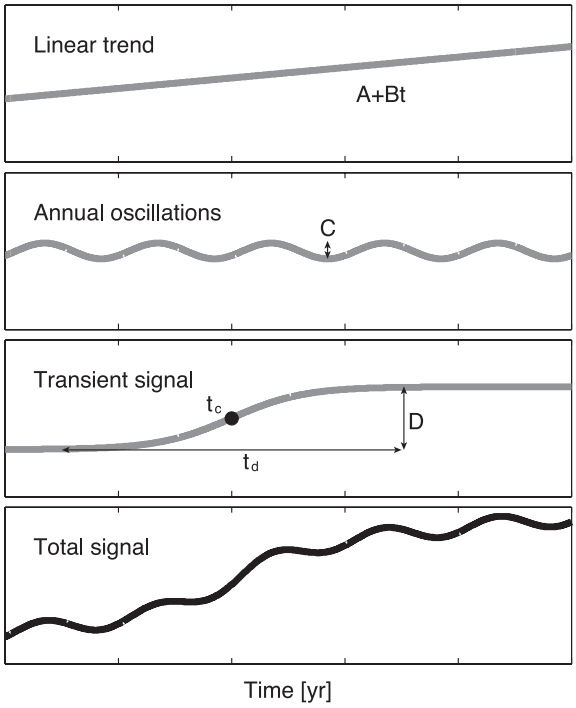

Figure 2. The CGPS time-series are modelled as a combination of a linear trend, annual oscillations and a transient uplift signal at Theistareykir with amplitude D, central time t_c and transient time t_d.

therefore assumed that the volcanic uplift occurred at constant rate during the CGPS observation period of 2006–2010 (Metzger *et al.* 2011). Here we use InSAR time-series analysis of ERS-1/2 satellite data to shed a better light on the uplift evolution at Theistareykir volcano.

We produced a number of interferograms out of 38 descending orbit scenes of the ERS-1 and 2 satellites spanning the time-period from 1992 to 2010 using the GAMMA software (GAMMA v1.0 2006). We then performed time-series analysis of the unwrapped interferograms using the π-RATE software package (Poly-Interferogram Rate And Time-series Estimator, 2009) that was developed by Biggs *et al.* (2007), Elliot *et al.* (2008) and Wang *et al.* (2009). The expected steady-state deformation, that is, due to plate spreading across the plate boundary and interseismic strain accumulation near the HFF, covers the whole scene and would be partially removed by the software during the correction of orbital errors. We preserve the cross-boundary signal by removing predicted line-of-sight (LOS) displacements from the interferograms before the orbital and topographical error correction and then add these predicted displacements back in again. The predicted displacements were derived from the deformation model of Metzger *et al.* (2011). The InSAR time-series processing steps are explained in more detail in Metzger & Jónsson (in preparation).

We extract an 800 $\times$ 800 m area from the InSAR time-series results, centred at Theistareykir volcano, and calculate the mean LOS displacement for each image acquisition date between 1992 and 2010 (Fig. 3). We find a linear rate between 1997 and 2007 that is caused by steady-state plate-boundary processes. Sudden uplift of $\sim$78 mm in LOS occurred in 2007, that seems to have ended in late 2008. Before 1997 we can see another transient which was most probably caused by deep magma accumulation at the Krafla volcanic system as reported by de Zeeuw-van Dalfsen *et al.* (2004).

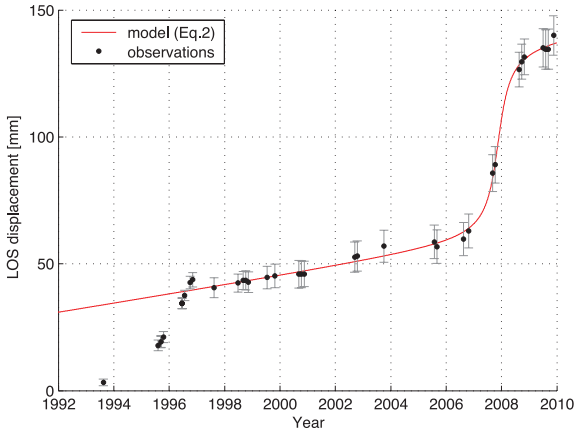

Figure 3. Temporal evolution of line-of-sight (LOS) displacement at Theistareykir central volcano, derived from InSAR time-series analysis. The results show two periods of uplift, one before 1997 and another between 2007 and 2009, as well as steady-state plate-boundary motion. The temporal deformation evolution after 1997 was modelled according to eq. (2).

We fit an inverse tangens functional to the temporal evolution of LOS displacements after 1997 (Fig. 3)

$$f(t) = A + Bt + D_0 \tan^{-1}\left(\frac{t - t_c}{t_d}\right), \quad (2)$$

that is defined with amplitude D_0, central time t_c, that is, the time of maximum uplift rate and transient time t_d. Using a non-linear optimization routine we find central time $t_c = 2007.88$ and transient time $t_d = 0.33$ yr. The total LOS displacement D_0 above the central volcano is 78 mm. If we use the Mogi source location and depth of 8.5 km derived by Metzger *et al.* (2011), this corresponds to a total Mogi volume change of 25×10^6 m^3. We then use the two parameters t_c and t_d and the Mogi source to correct for the transient volcanic deformation at each GPS observation point before estimating the linear GPS velocities in Sections 5.3 and 5.4.

5.2 Annual oscillations within CGPS time-series

The CGPS time-series show substantial annual oscillations, particularly in the vertical component (Grapenthin *et al.* 2006). After removing the volcanic uplift signal from the continuous time-series (Section 5.1) we then fit the following function,

$$f(t) = A + Bt + C\cos(2\pi t + \phi) \quad (3)$$

with a linear velocity term $A + Bt$ and an oscillation term C to each single component and station. Before the final non-linear optimization run, outliers were removed in two separate stages: First, all data points with a standard error three times larger than the mean error were dismissed. This affected only a couple of data points. After a first optimization run we excluded also all data points with a misfit three times larger than the mean misfit. The amount of excluded data for each station-component was never larger than 4 per cent. With a second optimization run we extracted the CGPS velocities of the cleaned data set. The resulting phase shift and amplitude parameters are plotted in Fig. 4 and show clearly, how the vertical component contains the strongest oscillation signal with a maximum value in winter time ($\phi = 0$). For the east and north component the amplitude is much smaller and thus not as nicely aligned with its mean value. However it is interesting to see that the mean phase shift for the east and north components differ from the vertical component with a maximum in October and September, respectively. The average rms

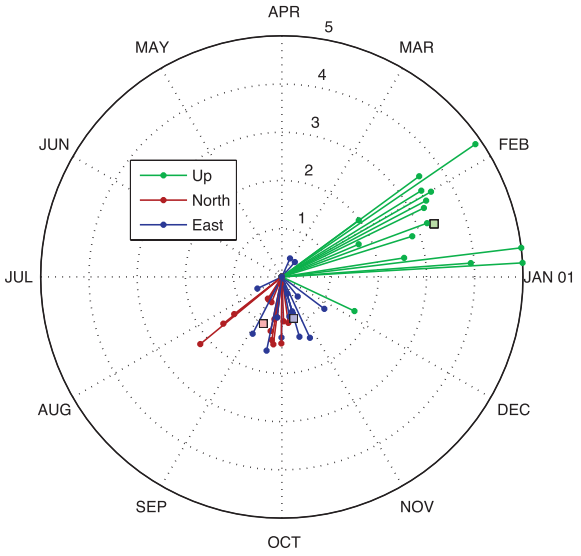

Figure 4. Phasor plot of estimated annual oscillation peaks and amplitudes (in mm) in the CGPS time-series. The squares mark the weighted mean of the peak shift and amplitude for each component.

values for the residuals of the time-series after removing the model described in eq. (3) are 1.5 mm for the horizontal component and 5.1 mm for the vertical component (Fig. 5).

5.3 Estimation of the EGPS velocities

The campaign data have always been acquired during summers so we ignore possible influence from annual oscillations. After correcting the EGPS time-series for the transient volcanic signal at Theistareykir we estimate the velocity for each station-component. For the EGPS data points we get a mean standard deviation from the assumed linear model of 3.4 mm for the horizontal and 22.3 mm for the vertical components (Fig. 5). The velocity variance was scaled by $1/T^2$, where T is the total duration of each time-series (Geirsson *et al.* 2006; Metzger *et al.* 2011).

The EGPS data set was analysed independently with both the BERNESE V5.0 and the GAMIT-GLOBK software packages as discussed in Section 4.2. To estimate the interseismic velocities of the EGPS stations we used SNX-files obtained from the BERNESE processing and the time-series resulting from the GLOBK analysis. Within GAMIT processing the data were already cleaned from potential outliers. This was not the case for the BERNESE data set where all data were processed and we therefore applied a visual quality control in the velocity estimation process to eliminate outliers in each time-series.

The resulting BERNESE and GAMIT velocity fields match well within uncertainties. We find that the velocities derived from GAMIT point slightly more towards the south (mean shift: 0.6 ± 0.6 mm yr^{-1}) and the east (0.3 ± 0.6 mm yr^{-1}) than the BERNESE solutions. The vertical components of GAMIT also show less upward motion (2.1 ± 1.5 mm yr^{-1}). Although this indicates a slight shift between the two network solutions we consider it as neglectable. The standard deviations of the shifts are larger than the shift itself, and what is more important, we account for a possible reference frame offset in our modelling in any case. The EGPS velocities we used in the modelling (Section 6) were obtained using the GAMIT-GLOBK software (Table 3).

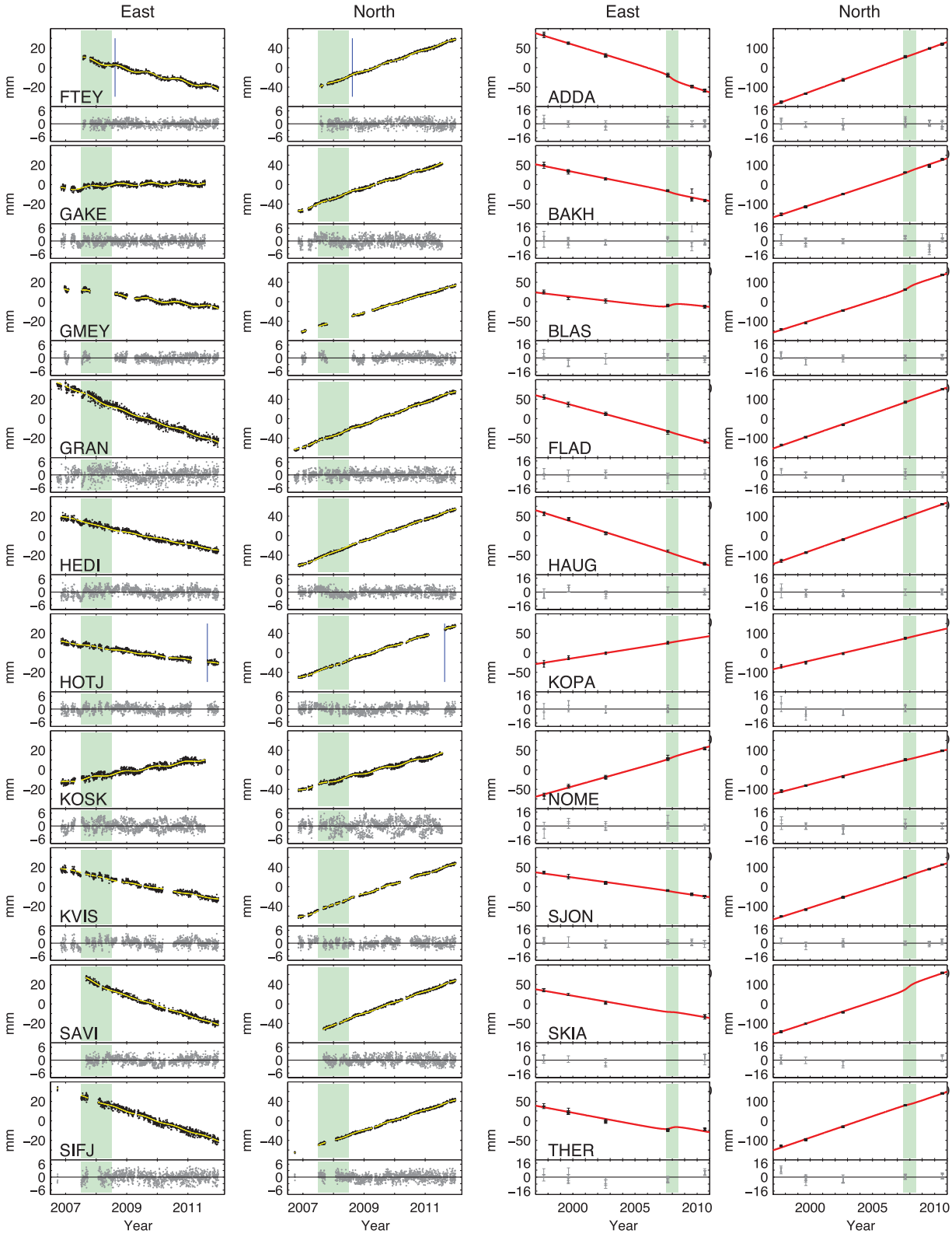

Figure 5. A selection of continuous (left-hand panel) and campaign (right-hand panel) horizontal GPS time-series (black dots, for station location refer to Fig. 1). The model prediction (yellow/red) accounts for steady inter seismic deformation, the volcanic uplift transient at Theistareykir in 2007–2009 (shaded in green) and seasonal oscillation (for CGPS data). Residuals are shown in the lower part of each subfigure (grey dots). The CPGS data are corrected for antenna changes (indicated by blue lines).

Table 3. Station abbreviations, coordinates, observed and modelled GPS velocities from continuous GPS stations 2006–2011 (upper part) and from EGPS data from 1997 to 2010 (lower part). The velocities are corrected for the volcanic uplift transient at Theistareykir in 2007–2009 and seasonal oscillation (Section 5) and represent the interseismic plate-boundary deformation. The reference frame is based on stable North America (MORVEL, DeMets *et al.* 2010) but slightly modified using an auxiliary model parameter (Section 6).

Station abbreviation	Latitude (°N)	Longitude (°W)	Observed velocities			Modelled velocities	
			East (mm yr^{-1})	North (mm yr^{-1})	Up (mm yr^{-1})	East (mm yr^{-1})	North (mm yr^{-1})
AKUR	65.68543	18.12248	1.7 ± 0.3	0.4 ± 0.3	3.9 ± 1.0	0.8	−0.2
ARHO	66.19307	17.10904	8.5 ± 0.2	−4.0 ± 0.3	0.0 ± 0.7	7.6	−2.8
FTEY	66.16032	17.84792	4.6 ± 0.3	−1.0 ± 0.3	−0.3 ± 1.1	4.7	−1.6
GAKE	66.07809	16.76466	11.5 ± 0.3	−3.9 ± 0.4	2.0 ± 1.2	9.9	−4.0
GMEY	66.53897	18.01901	7.6 ± 0.2	−3.9 ± 0.2	−2.9 ± 1.1	8.5	−2.1
GRAN	65.91866	17.57861	1.1 ± 0.4	−0.1 ± 0.3	3.0 ± 1.2	1.6	−0.5
HEDI	66.08072	17.30945	5.3 ± 0.3	−1.4 ± 0.3	1.3 ± 1.1	5.7	−2.3
HEID	65.38085	14.54095	19.3 ± 0.3	−8.5 ± 0.3	4.3 ± 0.9	18.8	−6.7
HOTJ	66.16166	17.24426	7.2 ± 0.3	−3.0 ± 0.3	−0.1 ± 1.1	6.9	−2.6
KOSK	66.30325	16.44343	16.0 ± 0.4	−7.6 ± 0.5	2.3 ± 1.1	16.5	−7.4
KVIS	66.10075	17.27171	5.8 ± 0.3	−2.6 ± 0.3	0.2 ± 1.0	6.2	−2.5
MYVA	65.64232	16.89135	11.5 ± 0.2	0.4 ± 0.3	1.0 ± 0.9	–	–
RHOF	66.46112	15.94671	17.3 ± 0.2	−7.9 ± 0.2	0.5 ± 0.9	18.3	−6.9
SAVI	65.99319	17.37610	1.6 ± 0.3	−0.5 ± 0.3	2.2 ± 1.2	3.0	−0.9
SIFJ	66.13804	18.89935	1.8 ± 0.3	−2.0 ± 0.3	−2.2 ± 1.1	1.0	0.1
ADDA	65.87335	17.36474	1.6 ± 0.2	0.5 ± 0.2	3.2 ± 3.7	1.9	−0.6
AEDA	65.98403	17.41486	2.2 ± 0.2	−0.7 ± 0.4	−0.5 ± 1.9	2.6	−0.8
AUDB	66.09650	16.95311	6.9 ± 0.3	−3.6 ± 0.4	1.3 ± 1.7	7.6	−3.1
AUSB	65.71412	16.53632	16.7 ± 0.3	−6.0 ± 0.3	7.1 ± 1.9	16.1	−6.2
BAKH	66.07600	17.35812	4.9 ± 0.4	−1.7 ± 0.4	0.1 ± 2.0	5.3	−2.1
BANG	66.14436	16.96801	7.6 ± 0.2	−4.0 ± 0.2	−3.0 ± 2.9	7.7	−3.1
BAUS	66.03179	17.25267	4.7 ± 0.2	−2.2 ± 0.4	0.8 ± 2.0	4.8	−1.9
BLAS	65.96293	16.87685	7.4 ± 0.3	−2.7 ± 0.2	4.8 ± 2.2	7.4	−3.2
BREV	66.19273	17.13735	8.0 ± 0.3	−3.3 ± 0.3	−0.1 ± 1.7	7.5	−2.7
FLAD	66.10728	17.89832	2.9 ± 0.2	−0.5 ± 0.2	−3.3 ± 1.7	2.8	−0.7
FLAT	66.15807	17.85308	4.7 ± 0.4	−0.8 ± 0.2	−4.0 ± 1.9	4.6	−1.5
GAUR	66.08112	16.77020	11.0 ± 0.3	−4.1 ± 0.2	−0.5 ± 1.8	9.8	−3.9
GEIR	65.89674	17.56457	1.6 ± 0.4	0.1 ± 0.3	0.0 ± 2.7	1.6	−0.5
GREN	65.97315	18.22341	1.1 ± 0.2	−0.8 ± 0.4	−0.9 ± 2.2	1.0	−0.2
HAHN	66.44703	16.46671	16.5 ± 0.2	−7.7 ± 0.3	−2.0 ± 1.7	17.7	−7.0
HAMH	65.85531	17.05957	2.1 ± 0.3	0.5 ± 0.3	3.0 ± 1.5	3.2	−1.2
HAST	65.92881	16.44621	18.4 ± 0.3	−5.5 ± 0.3	5.5 ± 1.4	16.3	−6.6
HAUG	65.93853	18.33757	1.6 ± 0.2	−0.3 ± 0.2	−0.2 ± 1.4	0.9	−0.1
HEHO	66.04866	16.95689	6.5 ± 0.3	−3.3 ± 0.2	2.9 ± 2.9	7.3	−3.1
HELL	65.96203	17.04041	5.4 ± 0.2	−3.4 ± 0.3	3.5 ± 1.9	5.0	−2.0
HOGI	65.96028	17.86680	1.1 ± 0.4	−0.6 ± 0.3	−3.4 ± 2.3	1.4	−0.3
HOLL	66.06405	16.66063	10.4 ± 0.3	−4.1 ± 0.3	−4.9 ± 1.6	12.2	−5.1
HOVA	65.96841	17.14862	3.5 ± 0.2	−2.0 ± 0.3	2.7 ± 2.0	4.1	−1.4
HUSA	66.04934	17.30522	4.7 ± 0.1	−1.8 ± 0.3	0.6 ± 1.8	4.9	−2.0
HVIT	65.69022	16.77528	9.3 ± 0.2	−0.4 ± 0.3	−2.8 ± 1.5	–	–
KJAH	65.92858	17.44461	1.7 ± 0.3	0.1 ± 0.3	0.3 ± 1.3	2.0	−0.6
KOPA	66.29180	16.43112	16.1 ± 0.3	−8.1 ± 0.5	−3.7 ± 2.4	16.4	−7.3
KRAF	65.71405	16.73026	6.1 ± 0.3	−4.9 ± 0.2	1.3 ± 0.9	–	–
LAUA	66.09451	18.65467	1.3 ± 0.3	−1.3 ± 0.2	−1.1 ± 2.1	1.1	0.0
LAUD	66.05507	17.34755	4.6 ± 0.4	−1.8 ± 0.4	4.3 ± 2.0	4.8	−1.8
LEDH	66.07237	18.07544	1.4 ± 0.3	−0.2 ± 0.2	−3.6 ± 1.7	1.7	−0.3
LYNG	66.03821	16.56920	12.7 ± 0.2	−4.7 ± 0.2	2.3 ± 1.6	13.9	−6.0
MEYJ	66.00776	17.26272	3.6 ± 0.3	−1.3 ± 0.1	−0.8 ± 1.6	4.1	−1.5
NOME	65.77323	16.34167	19.9 ± 0.3	−6.6 ± 0.2	5.2 ± 1.7	17.3	−6.5
NOMO	65.87919	16.69328	12.8 ± 0.2	−4.8 ± 0.2	4.4 ± 2.1	10.6	−5.3
RAND	65.79436	16.99340	3.5 ± 0.3	−1.1 ± 0.4	5.9 ± 2.0	3.9	−1.5
RAUH	65.95851	16.97372	5.5 ± 0.3	−2.4 ± 0.2	1.7 ± 1.6	5.8	−2.4
SAEL	65.96106	17.02178	5.4 ± 0.4	−2.4 ± 0.2	−0.0 ± 2.7	5.2	−2.1
SJON	66.15721	17.24376	6.9 ± 0.2	−2.6 ± 0.1	−0.3 ± 1.6	6.9	−2.6
SKIA	65.94542	16.99155	5.6 ± 0.3	−2.1 ± 0.2	2.2 ± 0.6	5.2	−2.1
SKIB	65.94481	16.99433	5.6 ± 0.3	−2.5 ± 0.4	3.3 ± 0.8	5.2	−2.0
SKIC	65.93308	17.00066	5.7 ± 0.5	−1.7 ± 0.4	4.1 ± 1.4	4.8	−1.8
SKID	65.93374	16.99646	5.4 ± 0.5	−1.7 ± 0.3	2.9 ± 0.8	4.9	−1.9
THER	65.88470	16.96364	5.1 ± 0.3	−1.0 ± 0.3	3.9 ± 1.5	4.5	−1.6
THRI	65.98022	17.00242	5.7 ± 0.2	−3.3 ± 0.4	−1.0 ± 1.7	5.9	−2.5
VORD	66.13526	16.35729	16.4 ± 0.1	−6.2 ± 0.1	1.3 ± 2.2	16.9	−6.8

5.4 Interseismic deformation in North Iceland

The estimated velocities and uncertainties for both the CGPS and EGPS stations are plotted in Fig. 6 in a reference frame originally based on stable North American Plate (MORVEL, DeMets *et al.* 2010), but modified with a small offset estimated in the modelling (Section 6). This correction was necessary for the modelling as GPS points located on the North American Plate, that is, southwest of

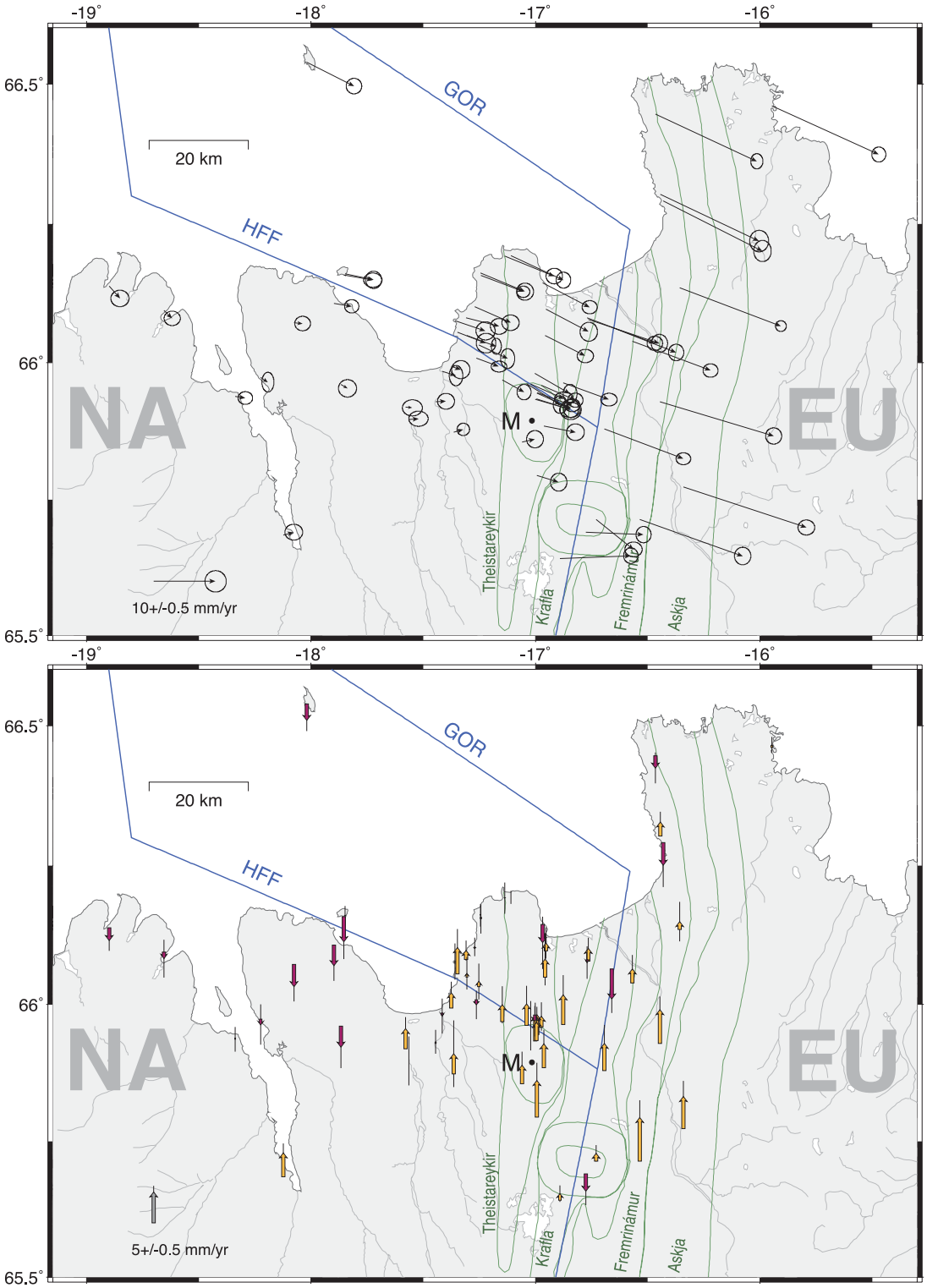

Figure 6. Horizontal (top) and vertical (bottom, purple: subsidence, yellow: uplift) GPS velocities with 95 per cent (top) and 68 per cent (bottom) confidence levels, after correcting for the Theistareykir uplift transient, simulated with the Mogi source M. Green lines outline fissure swarms and central volcanoes. The blue lines indicate the segments of the interseismic deformation model. The reference frame of the upper figure is based on fixed North America (MORVEL), but slightly modified with an offset vector of ∼4 mm yr^{-1} obtained from the modelling (Section 6).

Table 4. The best-fitting model parameters in comparison to the results of previous studies. The fault-parallel slip rate along the two HFF segments (Fig. 1) is derived from the partial transform motion parameter and the parameter describing amplitude and azimuth of the relative plate motion. The studies denoted with an asterisk (∗) share parts of the data set.

Data type Acquisition period	CGPS/EGPS∗, [a] 1997–2011	CGPS∗, [b] 2006–2010	CGPS∗, [c] 2001–2004	EGPS[d] 1993–2004	EGPS∗, [e] 1997–2002	InSAR[f] 1993–1999	Seismicity[g] 1994–1998	Geology[h] 7–9 Myr
Locking depth HFF (km)	$6.2^{+0.8}_{-0.7}$	$6.3^{+1.7}_{-1.2}$		4–15	>10–12		10–12	
Partial motion HFF (per cent)	33.4 ± 1.4	$33.9^{+3.1}_{-3.2}$	40					
Slip HFF1 (mm yr^{-1})	6.8 ± 0.3	$6.6^{+0.7}_{-0.6}$	∼7	<5	∼8			<7-8
Slip HFF2 (mm yr^{-1})	6.6 ± 0.3	$6.6^{+0.7}_{-0.6}$	∼7	<5	∼8			<7-8
Locking depth Ridge (km)	3.2 ± 0.2	$4.8^{+1.6}_{-1.1}$		5 ± 2		4.6		
Plate spreading (mm yr^{-1})	$20.3^{+0.4}_{-0.3}$	$19.6^{+0.8}_{-0.6}$		23 ± 2		25–34		
Spreading azimuth (°E)	109.4 ± 0.7	$115.1^{+1.2}_{-1.6}$						
Mogi volume (10^6 m^3)	25	$9.4^{+1.2}_{-1.0}$						

[a]This study; [b]Metzger *et al.* (2011); [c]Geirsson *et al.* (2006); [d]Árnadóttir *et al.* (2009); [e]Jouanne *et al.* (2006); [f]de Zeeuw-van Dalfsen *et al.* (2004); [g]Rögnvaldsson *et al.* (1998); [h]Sæmundsson (1974).

Húsavík, are not entirely stable in the North American reference frame and show a 2–4 mm yr^{-1} motion to the northwest. A similar motion pattern has been seen in previous studies (e.g. Árnadóttir *et al.* 2009) and it seems to apply to all GPS stations in Northwest Iceland, indicating a local reference frame problem.

We find that the TFZ covers the full plate motion of 18 mm yr^{-1} and that the deformation gradient across the NVZ is particularly strong (Fig. 6). All data vectors are more or less perpendicular to the orientation of the NVZ, except for stations close to Krafla central volcano that are influenced by local subsidence. Station velocities south of Skjálfandi Bay towards the northern tip of Tjörnes Peninsula gradually increase, indicating a locked HFF (see Fig. 1 for geographic locations).

Due to potential inconsistencies of the antenna height measurements the vertical deformation rates of EGPS data have to be interpreted with caution. North of Krafla central volcano a broad uplift of up to 6 mm yr^{-1} is apparent (Fig. 6). This signal coincides with uplift seen in InSAR data during 1993–1999 (de Zeeuw-van Dalfsen *et al.* 2004) that was thought to be caused by deep magma accumulation north of Krafla central volcano. At Krafla (relative) subsidence is visible, which is still ongoing but has been slowly decaying since the end of the Krafla rifting episode (Sturkell *et al.* 2008).

6 MODELLING

We describe the surface deformation of the TFZ as it has been observed by episodic and continuous GPS measurements during the last 14 yr with an interseismic back-slip model. This model consists of a set of nine planar plate-boundary segments with a fixed (Cartesian) geometry in an elastic half-space, as described by Metzger *et al.* (2011). The location of the plate boundary segments is shown in Fig. 1. The boundary follows roughly the Krafla fissure swarm in the south, then separates into two subparallel discontinuities along the HFF1 and 2 and the Grímsey Oblique Rift (GOR) that again reunite north of the TFZ at the Kolbeinsey Ridge. The plate-boundary deformation is described by superimposing reverse slip ('back-slip') on the locked part of the plate boundary onto rigid plate motion. The model does not allow for any rotation, because the slip on each model segment is uniform and is defined by the overall relative plate motion. Unlike in our previous study we do not include volcanic inflation at Theistareykir in the modelling, as we already eliminated this transient signal in the time-series analysis (Section 5). Otherwise, the model parameter optimization and error estimation procedures follow Metzger *et al.* (2011). The model parameter uncertainties are estimated by stochastically propagating the data errors through the modelling and do therefore not include the impact of model assumptions and simplifications. We here refer to this method as 'error propagation' and compare it to a second, independent uncertainty estimation, based on Bayesian estimation (Section 6.1).

The model segments are described by 10 parameters each, but many of them are constrained due to (1) the fixed location and vertical dip, (2) only two types of locking depths for the strike-slip segments (HFF1/2 and GOR in Fig. 1) and 'rift-type' segments (all other segments) and (3) no dip-slip motion. The key parameter we solve for is the locking depth of the HFF (Table 4). This value, along with the fault's length, determines the size of the locked HFF plane. Additional parameters are the locking depth of the ridge segments, the partitioning of transfer motion among the two lineaments HFF and GOR and the magnitude and azimuth of the overall plate spreading motion (Table 4). Two auxiliary parameters allow for a small shift of the North American reference frame into a model frame, which assumes a stable reference point southwest of the HFF. Together, the spreading vector and the partitioning of motion between the HFF and GOR define the slip-rate on the HFF. The slip-rate provides information about the stressing rate on a fault plane since the last large earthquake and gives, together with the locking-depth, an estimation of the seismic potential of this fault plane.

We include horizontal velocity components of all the CGPS and EGPS stations in the model parameter optimization (Table 3, except for one CGPS and two EGPS stations located near Krafla central volcano (MYVA/KRAF/HVIT). These stations are influenced by local subsidence at Krafla, which we do not account for in our model, because it is far from the HFF and does not influence near-fault velocities.

We find a locking depth for the HFF (and the GOR) of 6.2 and 3.2 km for the ridge segments. The total relative plate motion of 20.3 mm yr^{-1} with an azimuth of 109.4 °E is separated between the HFF and the GOR in a ratio of 33/67 per cent. The resulting data fit obtained by the best-fitting model parameters (Table 4) is in general

very good (Fig. 8, Table 3), except for the area north of Krafla central volcano where the steady-state interseismic deformation is slightly modified by uplift and extension. This is presumably due to deep magma accumulation during 1993–1999 (de Zeeuw-van Dalfsen *et al.* 2004).

6.1 Validation of the uncertainty estimation using a Bayesian estimation

We estimated the uncertainties of the best-fitting model parameters (Table 4) by analysing outcomes of 10 000 optimization runs with slightly modified ('noisy') input data. This method of estimating parameter uncertainties only considers the errors in the input data, but does not include errors from the modelling procedure or due to model simplifications. The resulting model parameter uncertainties should therefore be regarded as minimum uncertainties. Now, we validate this method of error propagation by applying Bayesian estimation, which provides a posterior probability distribution over the model parameters given the recorded data and serves as an independent assessment of the model.

We assume a linear M-dimensional model space $\mathcal{M}$, and a linear D-dimensional data space $\mathcal{D}$. The forward operator between these two spaces g, is assumed to be only mildly non-linear. The recorded measurements $\mathbf{d}$ and model parameters $\mathbf{m}$ are assumed to be realizations of the random variables D and M such that

$$\mathbf{d} = g(\mathbf{m}) + \epsilon, \tag{4}$$

where ϵ is a realization of stochastic noise. The posterior density in the model space is calculated according to Bayes' formula, here given in the form of Tarantola (2005)

$$\sigma_{\mathcal{M}}(\mathbf{m}) = kL(\mathbf{m})\,\rho_{\mathcal{M}}(\mathbf{m}), \tag{5}$$

where k serves as a normalization constant and $\rho_{\mathcal{M}}(\mathbf{m})$ represents the prior beliefs held of the parameters. The prior was chosen to be separately uniform distributions on every parameter m_{i} between two physically chosen bounding values $m_{\mathrm{i}}^{\min} < m_{\mathrm{i}} < m_{\mathrm{i}}^{\max}$. The likelihood function

$$L(\mathbf{m}) = \int_{\mathcal{D}} \rho_{\mathcal{D}}\,\theta(\mathbf{d}|\mathbf{m})\,\mathrm{d}\mathbf{d} \tag{6}$$

gives a measure of how good a model $\mathbf{m}$ is for explaining the data. $\rho_{\mathcal{D}}$ is the prior information on the data, and $\theta(\mathbf{d}|\mathbf{m})$ represents the correlation between the data and model parameters. Assuming the theoretical relationship between model parameters and data to be exact, $\theta(\mathbf{d}|\mathbf{m}) = \delta[\mathbf{d} - g(\mathbf{m})]$, allows to solve eq. (5). From the independence of ϵ and $\mathbf{m}$ in eq. (4), and from the assumption of Gaussian errors it follows that (Tarantola 2005)

$$\sigma_{\mathcal{M}} \propto \rho_{\mathcal{M}}(\mathbf{m}) \exp\left\{-\frac{1}{2}[\mathbf{d} - g(\mathbf{m})]^T \Sigma^{-1}[\mathbf{d} - g(\mathbf{m})]\right\}. \tag{7}$$

This density $\sigma_{\mathcal{M}}$ must then be evaluated by a Markov Chain Monte Carlo (MCMC) method due to the high dimensionality of model space $\mathcal{M}$. An MCMC algorithm is an algorithm for constructing a Markov chain with an equilibrium distribution equal to a given probability density function. The Metropolis–Hastings (M–H) algorithm (Hastings 1970) is an MCMC algorithm that picks the following state from a proposal distribution that is simpler than the sampled distribution, but uses a condition for rejecting unlikely states with greater probability to more likely ones. To find suitable parameters for this proposal distribution we first used a parameter-free MCMC algorithm called the Gibbs sampler described in Geman & Geman (1984). The Gibbs sampler iteratively samples

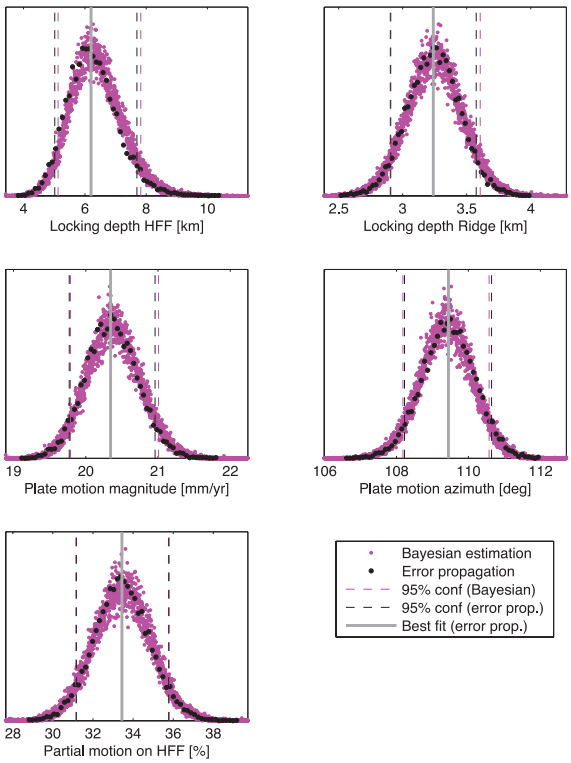

Figure 7. Estimations of the posterior marginal probability density functions for the TFZ model parameters using two different methods: error propagation and Bayesian estimation.

the conditional distributions of each variable, making it considerably slower for the problem at hand that lacks simple conditional distributions.

The M–H algorithm was started as multiple chains from arbitrary non-zero starting points in the model space. The first third of every chain is discarded to ensure convergence. The remaining samples are treated for autocorrelation by thinning, where only every τth sample was picked, so that samples τ steps apart are uncorrelated. τ was determined by the Geyer IMSE heuristic described in Geyer (1992). The remaining samples were considered representative of the posterior density (eq. 7).

The resulting marginal distributions of the model parameters from the Bayesian estimation are in a perfect agreement with the uncertainty estimation obtained by the error propagation (Fig. 7). Since one Bayesian estimation needs much less calculation time than obtaining a significant statistic from the error propagation method, we compare the 10 000 optimization runs of the error propagation method with one million of samples from the Bayesian estimation. This explains the difference in smoothness of the marginal distributions in Fig. 7. The 68 and 95 per cent-confidence levels do not deviate from each other more than 2 per cent for any parameters. This result is reassuring and confirms the validity of the error propagation method for determining the part of the model parameter uncertainties that is caused by errors in the input data.

7 DISCUSSION

The kinematic model presented in this paper is based on GPS time-series from 14 continuous GPS stations running since 2006 and 44 GPS markers that have been remeasured at least five times since 1997. We can compare the obtained result directly to our previous

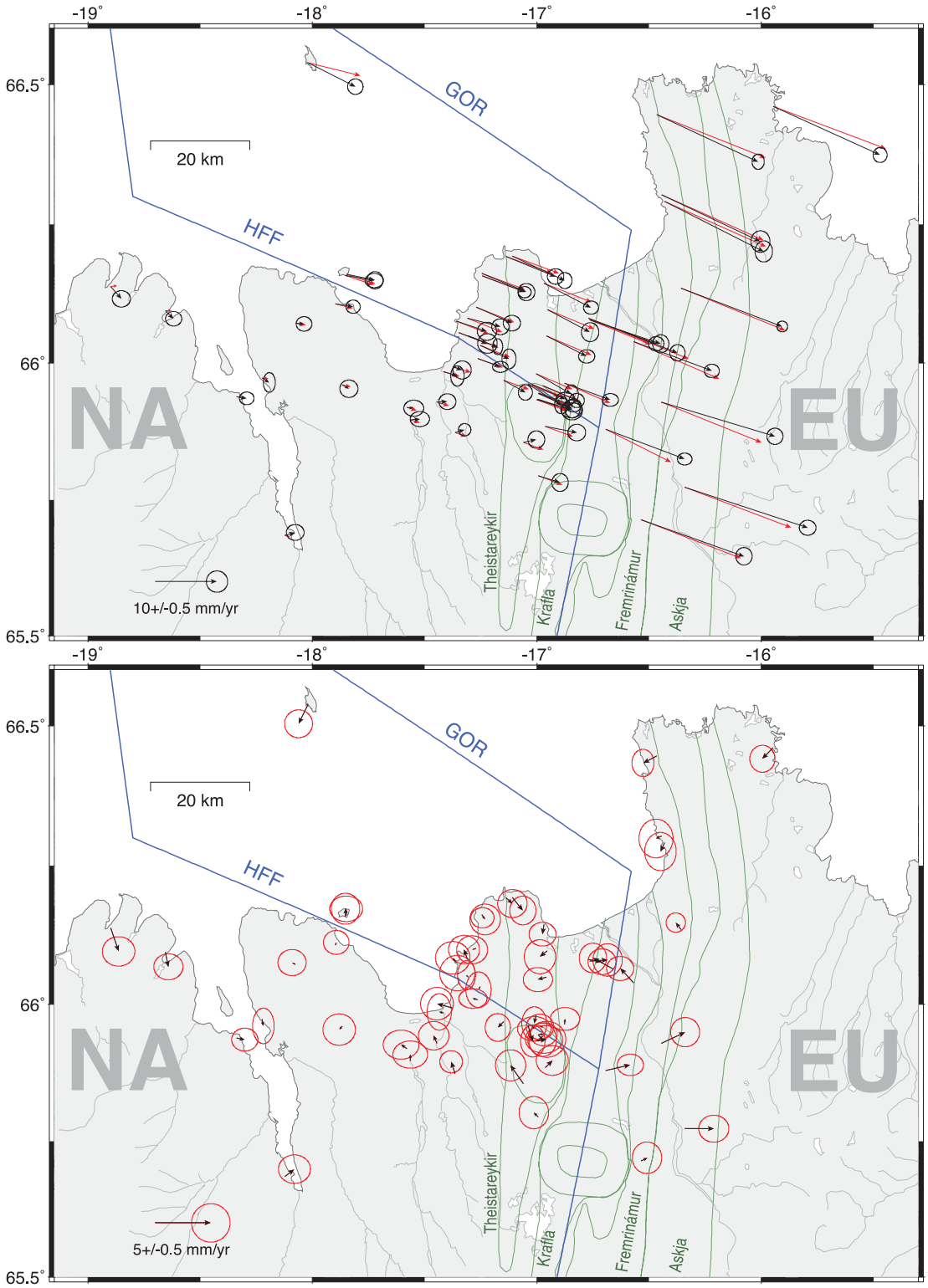

Figure 8. Velocity predictions (above) of the best-fitting model (red) in comparison to the observations with 95 per cent confidence level (black) and the residual signal between the two (below). Mind the different scale. The blue lines indicate the segments of the interseismic deformation model. The reference frame is based on a stable North America but modified with shift parameters obtained from the modelling (Chapter 6).

results (Metzger *et al.* 2011) where we used only the 14 CGPS data points (Table 4). The CGPS stations lie primarily on a profile across the two lineaments HFF and GOR and are sparse near the volcanic rift zone, which previously resulted in a poorly constrained ridge locking depth. The campaign GPS observations complement the CGPS network nicely and fill the gaps in the NVZ and on the Flateyarskagi peninsula southwest of the HFF (Fig. 1). This is the reason why the uncertainties of all our model parameters are at least 50 per cent smaller (Table 4) and why we get significant changes for the locking depth of the ridge segments (from 4.8 to 3.2 km) and

for the azimuth of plate motion (from 115°E to 109.4°E), which is now closer to the MORVEL plate motion azimuth of 105°E. The full plate motion increases again slightly from our previous best-fitting estimate of 19.6–20.3 mm yr^{-1}, which might be due to the broad uplift signal north of Krafla central volcano (Fig. 8) that also influences the horizontal displacement rates. All other parameters express only a slight change within or close to the uncertainty limits of our last study.

However, thanks to the improved data set, the estimated model parameter uncertainties have become so small that model uncertainties, which are not assessed in this study, would probably outweigh the propagated data uncertainties. In other words, if we use a different geometry for the plate boundary segments or another Earth model than an elastic half-space, the estimated model parameters would likely change beyond the current model parameter confidence bounds. Therefore, the estimated model parameter uncertainties should be regarded as minimum uncertainties as they only include the effect of the data errors. Further important model assumptions are: A complete stress release in 1872 when the last large earthquakes hit the HFF, a steady stress accumulation since then and a constant locking depth along the HFF segments. This last simplifying assumption is needed as the locking depth is mostly constrained by data points close to the southeastern end of the HFF, leaving no control over the northwestern part of the fault. Finally, we do not know exactly the effect of the Krafla rifting episode on the stress-regime of the HFF. Coulomb failure stress calculations derived from an opening dyke model at Krafla suggest a stress drop on the eastern part of the HFF, which might have relieved some of the accumulated stress on the fault (Maccaferri *et al.* 2012).

In comparison to our previous study, the implications on the seismic potential of the HFF fault do not change much and are in the same range of the 1755 and 1872 earthquakes. The slightly faster slip rate is neutralized by a slightly lower locking depth. To put the obtained modelling results in a general context, Table 4 compares the results of previous studies that provide information about the locking depth and slip rate of the HFF. Some of these studies are based in part on the same CGPS and EGPS data we use in this paper, while others are based on geological information (Sæmundsson 1974), seismicity analysis (Rögnvaldsson *et al.* 1998) or ISNET campaign GPS data (Árnadóttir *et al.* 2009). All these studies generally agree on the slip rate and locking depth of the HFF. A notable exception is the locking depth inferred from the results of Rögnvaldsson *et al.* (1998) that is almost twice as large as the estimates based on geodetic data (Metzger *et al.* 2011, and this study). The estimate from Rögnvaldsson *et al.* (1998) is deduced from relocated earthquakes with most of the epicentres close to the northwestern end of the HFF while the geodetically derived depths were constrained primarily by data points located near the southeastern end of the fault. The temperature gradient in Iceland can reach 150–200 °C km^{-1} at the flanks of the rift zone and decreases to 40–50 °C km^{-1} in the oldest crust in East and West Iceland (Palmason & Sæmundsson 1979). This means that the eastern end of the HFF that links to the NVZ likely has a higher temperature gradient than the Western, offshore end of the fault. Furthermore the seismic activity in Icelandic crust ceases at temperatures above 600–800 °C and the crust becomes partially molten at 1200 °C (Flóvenz & Sæmundsson 1993; Björnsson 2006). A map showing the estimated depth to the 1200 °C-isotherm in Iceland published in Flóvenz & Sæmundsson (1993) indicates increasing isotherm depth along the HFF from less than 15 km close to the triple junction at Theistareykir central volcano to more than 20 km at the northwestern end of the fault. The same applies for the heat flow that decreases from 140 to 175 mW m^{-2}, measured in boreholes close to the eastern end of the HFF in the Theistareykir area, to 80 mW m^{-2} on Flatey island. Assuming linear temperature gradient with depth, this would result in a variable thickness of the seismogenic zone and locking depth along the fault.

To calculate the seismic potential of the HFF we combine the fault slip-rate, length and locking depth of the HFF, which results in a tightly constrained moment that corresponds to a $M_w 6.81 \pm 0.04$ earthquake. The model segment of the HFF is connected to the Krafla rift segment but in reality the fault is ∼20 km shorter and ends in the Theistareykir fissure swarm (Fig. 1). As the seismic potential scales with the size of the fault plane and the accumulated slip (Aki 1966; Hanks & Kanamori 1979), the shorter fault length reduces the seismic potential by 20 per cent to $M_w 6.75$. On the other hand, if the locking depth is not uniform along the fault as our model assumes, but increases from 6.2 km in the east to 12 km in the West Rögnvaldsson *et al.* (1998), the fault loading increases by 15 per cent and the seismic potential becomes $M_w 6.85$. Given this variability, we therefore adjust the estimated seismic potential and its uncertainty to $M_w 6.8 \pm 0.1$.

8 CONCLUSIONS

The key objective of the work presented in this study was to derive a kinematic model of the Tjörnes Fracture Zone in North Iceland in order to estimate the locking depth and slip deficit of the HFF, and thus its seismic potential that has accumulated since the last large earthquakes in 1872. In our former paper we used only 14 CGPS stations to constrain parameters of an interseismic back-slip model of the plate boundary in North Iceland (Metzger *et al.* 2011). In this paper we almost quadruple the number of input GPS velocities by adding EGPS data dating back to 1997 and find similar optimal model parameters while all model parameter uncertainties are reduced by more than 50 per cent. We confirm our uncertainty estimations based on data error propagation with a Bayesian estimation. However, with the increased input data density, the derived model parameter uncertainties have become so small that the ambiguity caused by the choice of the model would probably outweigh the propagated data uncertainties and would likely significantly increase the overall model parameter uncertainties. Compared to our earlier study we find a slightly larger slip-rate and a slightly shallower locking depth of the HFF, resulting in an unchanged accumulated seismic moment, corresponding to a $M_w 6.8 \pm 0.1$ earthquake.

All model parameters, except for the ridge locking depth, changed within the estimated uncertainties. Relocated off-shore earthquakes along the western half of the HFF (Rögnvaldsson *et al.* 1998) suggest deeper locking (10–12 km) than what we obtain from on-land geodetic data near the eastern end of the fault (6.2 km). This possible along-strike variation in locking depth is supported by significant change in thermal gradient along the fault from a high gradient of 80 °C km^{-1} near the NVZ in the east to probably ∼50 °C km^{-1} in the west. If the locking depth increases gradually from 6.2 km in the east to 12 km in the west, it would mean that the accumulated stress is ∼15 per cent higher than estimated above, or equivalent to a $M_w 6.85$ earthquake.

ACKNOWLEDGMENTS

The collection of EGPS data up to 2007 was conducted by Thierry Villemin and François Jouanne, with financial support of the French

Polar Institute IPEV (Program 316). IPEV also supported the installation of the CGPS stations at Arholt (ARHO) and Raufarhöfn (RHOF). François Jouanne processed the EGPS data with BERNESE and Sigrún Hreinsdóttir helped with the GAMIT processing. Gillis Danielsen developed the codes for the Bayesian estimation. Pascale Bascou, André Blanchard, Olivier Cavalié, Gillis Danielsen, Janik Deutscher, Alice Gabriel, Notker Metzger and Rob Smith assisted in the GPS campaigns 2007–2011. The Húsavík Academic Center allowed us to use their facilities during field work. Some figures were produced with the GMT public domain software (Wessel & Smith 1998). We thank two anonymous reviewers for their help in improving the paper.

REFERENCES

Aki, K., 1966. Generation and Propagagion of G Waves from the Niigata Earthquake of June 16, 1964. Part 2. Estimation of earthquake moment, released energy and stress-strain drop from the G wave spectrum, *Bull. Earth. Res. Inst.,* **44,** 73–88.

Árnadóttir, T., Lund, B., Jiang, W., Geirsson, H., Björnsson, H., Einarsson, P. & Sigurdsson, T., 2009. Glacial rebound and plate spreading: results from the first countrywide GPS observations in Iceland, *Geophys. J. Int.,* **177**(2), 691–716.

Biggs, J., Wright, T., Lu, Z. & Parsons, B., 2007. Multi-interferogram method for measuring interseismic deformation: Denali Fault, Alaska, *Gephys. J. Int.,* **170,** 1165–1179.

Björnsson, A., 1985. Dynamics of crustal rifting in NE Iceland, *J. geophys. Res.,* **90**(NB12), 151–162.

Björnsson, A., 2006. Temperature of the Icelandic crust: inferred from electrical conductivity, temperature surface gradient, and maximum depth of earthquakes, *Tectonophysics,* **447**(1-4), 136–141.

Dach, R., Hugentobler, U., Fridez, P. & Meindl, M., 2007. *Bernese GPS Software Version 5.0,* Stämpfli Publications AG, Bern.

de Zeeuw-van Dalfsen, E., Pedersen, R., Sigmundsson, F. & Pagli, C., 2004. Satellite radar interferometry 1993–1999 suggests deep accumulation of magma near the crust-mantle boundary at the Krafla volcanic system, Iceland, *Geophys. Res. Lett.,* **31**(13), 5–9.

DeMets, C., Gordon, R.G. & Argus, D.F., 2010. Geologically current plate motions, *Geophys. J. Int.,* **181**(1), 1–80.

Einarsson, P., 1976. Relative location of earthquakes in the Tjörnes fracture zone, *Soc. Sci. Islandica,* Greinar V 45–60.

Einarsson, P., 1991. Earthquakes and present-day tectonism in Iceland, *Tectonophysics,* **189**(1-4), 261–279.

Einarsson, P. & Sæmundsson, K., 1987. Earthquakes epicenters 1982-1985 and volcanic systems in Iceland, map accompanying the Festschrift, *Í hlutarins edli,* ed. Sigfusson, T.I. scale 1:750000, Meningarsjóður, Reykjavik, Iceland.

Elliot, J., Biggs, J., Parsons, B. & Wright, T., 2008. InSAR slip rate determination on the Altyn Tagh Fault, northern Tibet, in the presence of topographically correlated atmospheric delays, *Geophys. Res. Lett.,* **35**(L12309), doi:10.1029/2008GL033659.

Flóvenz, O.G. & Sæmundsson, K., 1993. Heat flow and geothermal processes in Iceland, *Tectonophysics,* **225**(1-2), 123–138.

Foulger, G.R., Jahn, C.H., Seeber, G., Einarsson, P., Julian, B.R. & Heki, K., 1992. Post-rifting stress-relaxation at the divergent plate boundary in Northeast Iceland, *Nature,* **358**(6386), 488–490.

GAMMA v1.0, 2006. *GAMMA Software Introduction,* GAMMA Remote Sensing research and Consulting AG, Gümligen, Switzerland, http://www.gamma-rs.ch.

Geirsson, H. *et al.*, 2006. Current plate movements across the Mid-Atlantic Ridge determined from 5 years of continuous GPS measurements in Iceland, *J. geophys. Res.,* **111**(B09407), doi:10.1029/2005JB003717.

Geman, S. & Geman, D., 1984. Stochastic relaxation, Gibbs distributions, and the Bayesian restoration of images, *IEEE Trans. Pattern Anal. Mach. Intell.,* **6,** 721–741.

Geyer, C.J., 1992. Practical Markov Chain Monte Carlo, *Stat. Sci.,* 473–511.

Grapenthin, R., Sigmundsson, F., Geirsson, H., Árnadottir, T. & Pinel, V., 2006. Icelandic rhythmics: annual modulation of land elevation and plate spreading by snow load, *Geophys. Res. Lett.,* **33**(L24305), doi:10.1029/2006GL028081.

Gudmundsson, A., Brynjolfsson, S. & Jonsson, M.T., 1993. Structural analysis of a transform fault-rift zone junction in North Iceland, *Tectonophysics,* **220,** 205–221.

Halldórsson, P., 2005. Jarðskjálftavirkni á Norðurlandi - Earthquake activity in N-Iceland. Greinarger. Veðurstofu Íslands, *IMO report 05021 (in Icelandic)*, p. 34.

Hanks, T.C. & Kanamori, H., 1979. Moment magnitude scale, *J. geophys. Res.,* **84**(NB5), 2348–2350.

Hastings, W.K., 1970. Monte Carlo sampling methods using Markov chains and their applications, *Biometrika,* **57**(1), 97–109.

Heki, K., Foulger, G.R., Julian, B.R. & Jahn, C.H., 1993. Plate dynamics near divergent boundaries - geophysical implications of postrifting crustal deformation in NE Iceland, *J. geophys. Res.,* **98**(B8), 14 279–14 297.

Herring, T.A., King, R.W. & McClusky, S.C., 2010a. Introduction to GAMIT/GLOBK, Release 10.4, Department of Earth, Atmospheric, and Planetary Sciences, Massachusetts Institute of Technology.

Herring, T.A., King, R.W. & McClusky, S.C., 2010b. GAMIT Reference Manual – GPS Analysis at MIT, Release 10.4, Department of Earth, Atmospheric, and Planetary Sciences, Massachusetts Institute of Technology.

Herring, T.A., King, R.W. & McClusky, S.C., 2010c. GLOBK Reference Manual – Global Kalman filter VLBI and GPS analysis program, Release 10.4, Department of Earth, Atmospheric, and Planetary Sciences, Massachusetts Institute of Technology.

Hofton, M.A. & Foulger, G.R., 1996. Postrifting anelastic deformation around the spreading plate boundary, North Iceland. 1. Modeling of the 1987-1992 deformation field using a viscoelastic earth structure, *J. geophys. Res.,* **101**(B11), 25 403–25 421.

Homberg, C., Bergerat, F., Angelier, J. & Garcia, S., 2010. Fault interaction and stresses along broad oceanic transform zone: Tjörnes Fracture Zone, north Iceland, *Tectonics,* **29**(TC1002), doi:10.1029/2008TC002415.

INMH, 1998. Tectonic Map of Iceland published by *Icelandic Institute of Natural History,* compiled by H. Jóhanesson and K. Sæmundsson, ed. Mál og menning, Reykjavik.

Jouanne, F., Villemin, T., Ferber, V., Maveyraud, C., Ammann, J., Henriot, O. & Got, J.L., 1999. Seismic risk at the rift-transform junction in north Iceland, *Geophys. Res. Lett.,* **26**(24), 3689–3692.

Jouanne, F., Villemin, T., Berger, A. & Henriot, O., 2006. Rift-transform junction in North Iceland: rigid blocks and narrow accommodation zones revealed by GPS 1997-1999-2002, *Geophys. J. Int.,* **167**(3), 1439–1446.

Maccaferri, F., Rivalta, E., Passarelli, L. & Jónsson, S., 2012. The stress shadow induced by the 1975-1984 Krafla rifting episode, *J. geophys. Res.,* submitted.

Magnúsdóttir, S. & Brandsdóttir, B., 2011. Tectonics of the peistareykir fissure swarm, *Jökull,* **61,** 65–79.

McMaster, R.L., Schilling, J.G.E. & Pinet, P.R., 1977. Plate boundary within Tjörnes Fracture Zone on northern Icelands insular margin, *Nature,* **269**(5630), 663–668.

Metzger, S., Jónsson, S. & Geirsson, H., 2011. Locking depth and slip-rate of the Húsavík Flatey fault, North Iceland, derived from continuous GPS data 2006-2010, *Geophys. J. Int.,* **187**(2), 564–576.

Mogi, K., 1958. Relations between the eruptions of various volcanoes and the deformations of the ground surfaces around them, *Bull. Earthq. Res. Inst., Univ. Tokyo,* **36,** 99–134.

Palmason, G. & Sæmundsson, K., 1979. Summary of conductive heat flow in Iceland, in *Terrestrial Heat Flow in Europe,* eds Cermak, V. & Rybach, L., Springer, Berlin, Heidelberg, Springer-Verlag, p. 218–220

Passarelli, L., Maccaferri, F., Rivalta, E., Dahm, T. & Boku, E., 2012. A probabilistic approach for the classification of earthquakes as "triggered" or "not triggered": application to the 13th Jan 1976 Kópasker Earthquake on the Tjörnes Fracture Zone, Iceland, *J. Seismol.,* **1383-4649,** 1–23.

Poly-Interferogram Rate And Time-series Estimator, 2009. V2.0b2. Available at: http://homepages.see.leeds.ac.uk/~earhw/pirate/.

Rögnvaldsson, S.T., Gudmundsson, A. & Slunga, R., 1998. Seismotectonic analysis of the Tjörnes Fracture Zone, an active transform fault in north Iceland, *J. geophys. Res.,* **103**(B12), 30 117–30 129.

Sæmundsson, K., 1974. Evolution of the Axial Rifting Zone in Northern Iceland and the Tjörnes Fracture Zone, *Geol. Soc. of America Bull.,* **85,** 495–504.

Sigurdsson, H. & Sparks, R.S.J., 1978. Rifting Episode in North Iceland in 1874-1875 and the Eruptions of Askja and Sveinagja, *Bull. Volcanol.,* **41**(3), 149–167.

Stefánsson, R., Gudmundsson, G.B. & Halldórsson, P., 2008. Tjörnes fracture zone. New and old seismic evidences for the link between the North Iceland rift zone and the Mid-Atlantic ridge, *Tectonophysics,* **447**(1-4), 117–126.

Sturkell, E., Sigmundsson, F., Geirsson, H., Ólafsson, H. & Theodórsson, T., 2008. Multiple volcano deformation sources in a post-rifting period: 1989–2005 behaviour of Krafla, Iceland constrained by levelling, tilt and GPS observations, *J. Volc. Geotherm. Res.,* **177**(2), 405–417.

Tarantola, A., 2005. *Inverse Problem Theory and Methods for Model Parameter Estimation,* Society for Industrial and Applied Mathematics, Philadelphia.

Thorgeirsson, O., 2012. Sögulegir jarðskáfltar á Norðurlandi—Historic Earthquakes in North Iceland (in Icelandic), University of Iceland, p. 80.

Thoroddsen, T., 1880. An account of volcanic eruptions and earthquakes which have taken place in Iceland within historical times, *Geol. Mag.,* **7**(10), 458–467.

Thoroddsen, T., 1925. Die Geschichte der isländischen Vulkane, *D. Kgl. Danske Vidensk. Selsk. Skrifter, Naturwidensk. og Mathem. Afd.,* **8**(9), 1–458.

Tryggvason, E., 1980. Subsidence events in the Krafla area, North-Iceland, 1975-1979, *J. Geophys.,* **47**(1-3), 141–153.

Tryggvason, E., 1984. Widening of the Krafla fissure swarm during the 1975-1981 volcano-tectonic episode, *Bull. Volc.,* **47,** 47–69.

Tryggvason, E., 1994. Surface deformation at the Krafla volcano, North Iceland, 1982-1992, *Bull. Volc.,* **56,** 98–107.

Völksen, C., 2000. Die Nutzung von GPS für die Deformationsanalyse in regionalen Netzen am Beispiel Islands, *PhD thesis,* Wissenschaftliche Arbeiten der Fachrichtung Vermessungswesen, Universität Hannover.

Wang, H., Wright, T. & Biggs, J., 2009. Interseismic slip rate of the northwestern Xianshuihe fault from InSAR data, *Geophys. Res. Lett.,* **36**(L03302), doi:10.1029/2008GL036560.

Wesnousky, S.G., 1986. Earthquakes, quaternary faults, and seismic hazard in California, *J. geophys. Res.,* **91**(B12), 2587–2631.

Wessel, P. & Smith, H.F., 1998. New improved version of the Generic Mapping Tools released, *EOS, Trans. Am. geophys. Un.,* **79**(47), 579.